tained from the spatial differentiation of the displacement distribution. The strain distribution was then reconstructed as an elasticity image and was displayed on the computer monitor. The program that was used for this reconstruction was developed at the University of Tsukuba (T.S.) (2–4).

Each pixel of the elasticity image was assigned one of 256 specific colors, depending on the magnitude of strain. The scale ranged from red for components with greatest strain (ie, softest components) to blue for those with no strain (ie, hardest components). Green indicated average strain in the ROI. These color-scale elasticity images were converted to translucent images and were superimposed on the corresponding B-mode images so that the investigator could easily recognize the relationship between strain distribution and the lesion on B-mode images at a glance. Color images were constructed automatically with the same image processing settings throughout the study. Image construction was performed by using a program developed by Hitachi Medical (T.M.) (9).

To obtain a still image for diagnosis, we replayed the recorded motion images and selected an image obtained in the early phase of compression because these images provided the best contrast. Normal breast tissue was displayed in the green range.

To classify elasticity images, we evaluated the color pattern both in the hypoechoic lesion (ie, the area that was hypoechoic or isoechoic relative to the subcutaneous fat [except for echogenic halo] on B-mode images) and in the surrounding breast tissue. On the basis of the overall pattern, we assigned each image an elasticity score on a five-point scale (Fig 1). A score of 1 indicated even strain for the entire hypoechoic lesion (ie, the entire lesion was evenly shaded in green) (Fig 2). A score of 2 indicated strain in most of the hypoechoic lesion, with some areas of no strain (ie, the hypoechoic lesion had a mosaic pattern of green and blue) (Fig 3). A score of 3 indicated strain at the periphery of the hypoechoic lesion, with sparing of the center of the lesion (ie, the peripheral part of lesion was green, and the central part was blue) (Fig 4). A score of 4 indicated no strain in the entire hypoechoic lesion (ie, the entire lesion was blue, but its surrounding area was not included) (Fig 5). A score of 5 indicated no strain in the entire hypoechoic lesion or in the surrounding area (ie, both the

Figure 4

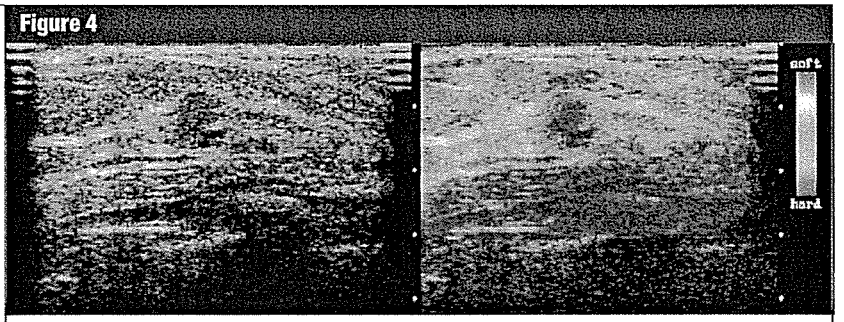

Figure 4: Lobular carcinoma in situ with elasticity score of 3 in 46-year-old woman. US images were obtained in transverse plane. Left: On conventional B-mode image, lesion was classified as BI-RADS category 3. Right: On elasticity image, the central part of the hypoechoic lesion was blue, and the peripheral part of the lesion was green.

Figure 5

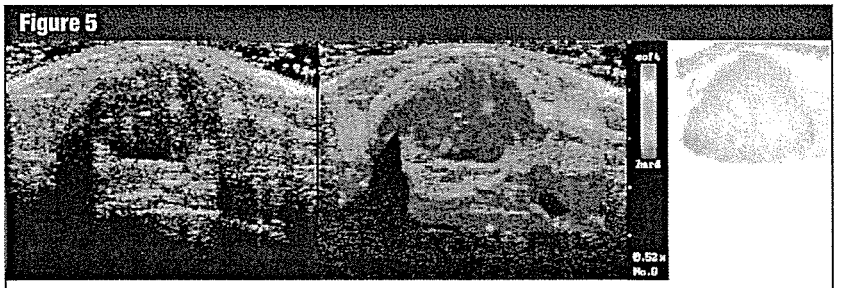

Figure 5: Nonscirrhous type invasive ductal carcinoma with elasticity score of 4 in 29-year-old woman. US images were obtained in transverse plane. Left: On conventional B-mode image, lesion was classified as BI-RADS category 5. Middle: On elasticity image, the entire hypoechoic lesion was blue. Right: Pathologic section of lesion is shown. (Hematoxylin-eosin stain; original magnification, ×1.)

Figure 6

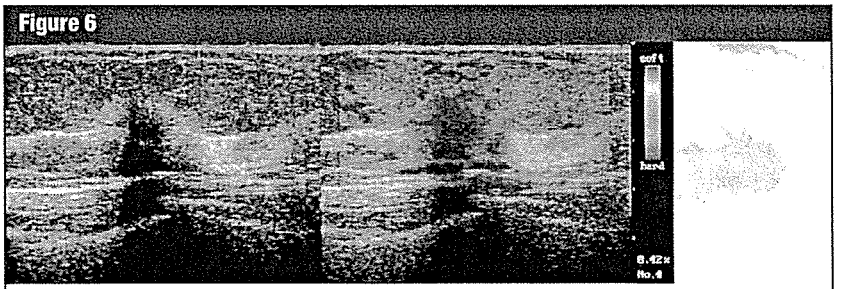

Figure 6: Scirrhous type invasive ductal carcinoma with elasticity score of 5 in 55-year-old woman. US images were obtained in sagittal plane. Left: On conventional B-mode image, lesion was classified as BI-RADS category 5. Middle: On elasticity image, both the entire hypoechoic lesion and its surrounding area were blue. Right: Pathologic section of lesion is shown. (Hematoxylin-eosin stain; original magnification, ×1.)

entire hypoechoic lesion and its surrounding area were blue) (Fig 6).

Scoring was performed by a surgeon (A.I.) who had 5 years of experience in evaluating breast US results according to the imaging patterns described (Fig 1). In the first stage of the study (from March 2002 to March 2003), scoring was performed in 57 lesions, with knowledge of the results of conventional US examination and the final pathologic diagnosis. In the second stage of the study (from April 2003 to September 2003), scoring was performed in 54 lesions, with knowledge of the results of physical examination and mammography but without knowledge of the results of conventional US examination and the final pathologic diagnosis.

Table 2

Final Pathologic Diagnosis in 111 Breast Lesions

Pathologic Diagnosis	No. of Lesions
Malignant lesions	52 (46.8)
Invasive ductal carcinoma	
Nonscirrhous	32 (28.8)
Scirrhous*	10 (9.0)
Ductal carcinoma in situ	9 (8.1)
Mucinous carcinoma	1 (0.9)
Benign lesions	59 (53.2)
ANDI†	24 (21.6)
Fibroadenoma	16 (14.4)
Intraductal papilloma	13 (11.7)
Complex cyst	2 (1.8)
Benign phyllodes tumor‡	2 (1.8)
Lobular carcinoma in situ	1 (0.9)
Granuloma	1 (0.9)

Note.—Numbers in parentheses are percentages.

* Defined as carcinoma that had a hard consistency because of excessive production of dense connective tissue.

† Indicates ANDI without fibroadenoma.

‡ Excisional biopsy was performed in both phyllodes tumors; tumors were proven with histologic analysis.

Figure 7

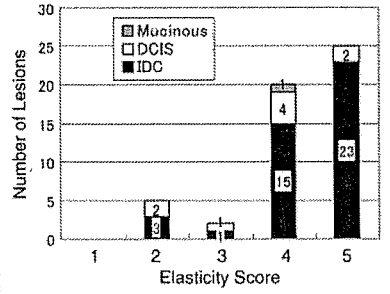

Figure 7: Bar graph demonstrates distribution of elasticity scores for malignant lesions. Numbers on bars indicate the number of lesions. *IDC* = invasive ductal carcinoma, *Mucinous* = mucinous carcinoma.

Figure 8

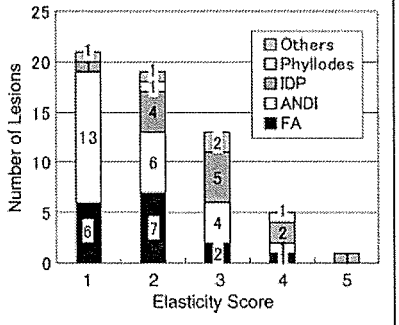

Figure 8: Bar graph demonstrates distribution of elasticity scores for benign lesions. Numbers on bars indicate the number of lesions. For the category termed *others*, lesions included complex cysts, lobular carcinoma in situ, and granulomas. *FA* = fibroadenoma, *IDP* = intraductal papilloma, *Phyllodes* = benign phyllodes tumor.

Statistical Analysis

We first compared malignant and benign lesions by *(a)* comparing the mean elasticity scores for real-time US elasticity images between malignant and benign lesions to determine the score for differentiating between these lesions and *(b)* comparing the elasticity scores between the three groups within each lesion size category (ie, 4–10 mm, 11–20 mm, and 21–30 mm) to assess the usefulness of this modality for various lesion sizes. All comparisons were made by using the Student *t* test.

Furthermore, we compared elasticity scores among the histologic subgroups of lesions by using an analysis of variance (Tukey-type multiple comparison) to assess the correspondence between the elasticity score and the compressibility of each histologic type, with pathologic diagnoses as a reference standard.

Finally, we evaluated the ability of the two imaging modalities to allow differentiation of malignant and benign lesions by using a receiver operating characteristic analysis to compare the area under the curve, sensitivity, specificity, and accuracy. Here, the standard proportion test was conducted for sensitivity, specificity, and accuracy. For the indices that did not show a statistically significant difference, we examined equivalence or noninferiority by using the Δ-equivalent test (10).

In addition, we used the χ^2 test to assess the presence of a significant difference between lesions scored in the first stage of the study and those scored in the second stage of the study; as previously noted, the conditions under which scoring was performed were somewhat different.

All statistical tests were performed by using commercially available software (Stat Mate 2000, version 3.01, ATMS, Tokyo, Japan and PASS 2002, NCSS, Kaysville, Utah). For all tests, a *P* value of less than .05 was considered to indicate a statistically significant difference.

Results

Pathologic Diagnoses

Final pathologic diagnoses are shown in Table 2. All breast cancers were diagnosed histologically by means of radical surgery, excisional biopsy, or needle biopsy. Of the 59 benign lesions, 18 were diagnosed at excisional biopsy, 19 at US-guided needle biopsy, and 22 at fine-needle aspiration cytology. Furthermore, all benign lesions remained unchanged during the follow-up period, which spanned more than 1 year.

Elasticity Scores

The distributions of elasticity scores for malignant lesions and benign lesions are shown in Figures 7 and 8, respectively. The mean elasticity score was significantly higher for malignant lesions (4.2 ± 0.9) than for benign lesions (2.1 ± 1.0) ($P < .001$).

Of the 52 malignant lesions, 45 (86%) lesions, including invasive ductal

carcinoma, had a score of 4 or 5. None of the lesions in this group had a score of 1. Of the 59 benign lesions, 40 (68%) lesions, including fibroadenomas and ANDI without fibroadenoma, had a score of 1 or 2 (score of 1, 21 lesions; score of 2, 19 lesions).

One (4%) of the 26 lesions with a score of 5 and five (20%) of the 25 lesions with a score of 4 were benign. Two (13%) of 15 lesions with a score of 3 and five (21%) of 24 lesions with a score of 2 were malignant. Of note, three of the malignant lesions with a score of 2 occurred in the first stage of our study.

The mean elasticity scores according to lesion size on B-mode images are shown in Table 3. For each lesion size category, the mean score was significantly higher for malignant lesions than for benign lesions ($P < .001$).

The distribution of elasticity scores for breast cancers according to their histologic subclassification is shown in Figure 9. The mean score was 3.7 ± 1.0 for DCIS, 4.2 ± 0.9 for invasive ductal carcinoma of nonscirrhous type, and 4.9 ± 0.3 for invasive ductal carcinoma of scirrhous type. There were no significant differences between the mean scores for invasive ductal carcinomas of scirrhous type and those for invasive ductal carcinomas of nonscirrhous type. The mean scores for nonscirrhous carcinoma and those for DCIS did not differ significantly. Mean scores for scirrhous carcinoma and those for DCIS, however, did differ significantly ($P < .05$). Of the five malignant lesions with a score of 2, two were DCIS and three were invasive ductal carcinomas of nonscirrhous type.

The distribution of elasticity scores for benign lesions according to their histologic characteristics is shown in Figure 10. The mean score was 1.9 ± 0.9 for fibroadenoma, 1.7 ± 0.9 for ANDI, and 2.9 ± 1.0 for intraductal papilloma. The mean scores for intraductal papilloma and those for ANDI differed significantly ($P < .01$). In contrast, there was no significant difference between the mean scores for fibroadenoma and those for ANDI or between the mean scores for intraductal papilloma and those for fibroadenoma.

There was no significant difference between the mean elasticity scores for intraductal papilloma and those for DCIS. However, the mean scores for other benign lesions (fibroadenoma and ANDI) and those for all subclasses of carcinomas differed significantly ($P < .001$ for each comparison).

Table 3

Mean Elasticity Score according to Lesion Diameter

Diameter (mm)*	Malignant	Benign	*P* Value†
4–10	3.9 ± 1.7 (9)	1.9 ± 0.9 (28)	<.001
11–20	4.4 ± 0.8 (27)	2.3 ± 1.2 (26)	<.001
21–30	4.2 ± 1.0 (16)	2.4 ± 0.6 (5)	<.001

Note.—Elasticity scores are presented as the mean ± standard deviation. Numbers in parentheses indicate the total number of lesions for each size category.

* Lesion diameter was determined at B-mode US and was measured to the nearest millimeter.

† Within each size category, the difference between elasticity scores for malignant and benign lesions was determined to be significant by using the Student *t* test.

Figure 9

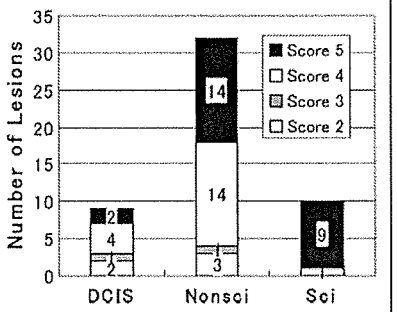

Figure 9: Bar graph demonstrates distribution of elasticity scores for breast cancers according to histologic subclassification. Numbers on bars indicate the number of lesions. *Nonsci* = invasive ductal carcinoma of nonscirrhous type, *Sci* = invasive ductal carcinoma of scirrhous type.

Figure 10

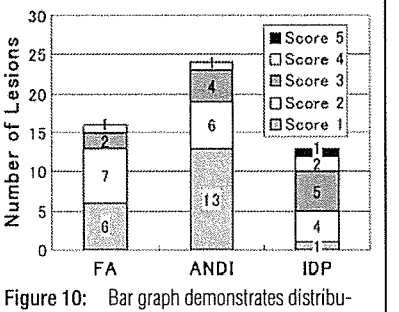

Figure 10: Bar graph demonstrates distribution of elasticity scores for benign lesions according to histologic subclassification. Numbers on bars indicate the number of lesions. *FA* = fibroadenoma, *IDP* = intraductal papilloma.

Figure 11

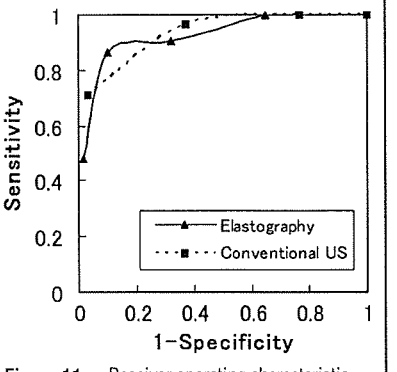

Figure 11: Receiver operating characteristic curves for elastography and conventional US. The area under the curve was almost the same for both elastography and conventional US (0.9185 and 0.9153, respectively). Statistical comparison was not possible because the number of lesions was insufficient.

Diagnostic Performance

Figure 11 shows the receiver operating characteristic curves for elastography and conventional US in differentiating malignant from benign legions. This bar graph shows that the maximum value of the sum of sensitivity and specificity for elastography is higher than that for conventional US. The area under the curve

for elastography was 0.9185, which is slightly higher than that for conventional US (0.9153).

The diagnostic performance of conventional US and of elastography at various cutoff points for the entire study period (stage one and stage two) is shown in Table 4. For elastography, sensitivity (86.5% [45 of 52]; 95% confidence interval: 77.3%, 83.5%), specificity (89.8% [53 of 59]; 95% confidence interval: 82.1%, 97.5%), and accuracy (88.3% [98 of 111]; 95% confidence interval: 82.3%, 94.3%) are shown, with the best cutoff point between elasticity scores of 3 and 4. According to the conventional method, a cutoff point is defined as best if it attains the maximum of value of sum of sensitivity and specificity. The sensitivity (71.2% [37 of 52]; 95% confidence interval: 58.8%, 83.5%), specificity (96.6% [57 of 59]; 95% confidence interval: 92.0%, 100.0%), and accuracy (84.7% [94 of 111]; 95% confidence interval: 78.0%, 91.4%) of conventional US are also shown in Table 4, with the best cutoff point between BI-RADS category 4 and 5. If another cutoff point is applied between BI-RADS category 3 and 4, then sensitivity moves to 96.2% (50 of 52), specificity to 62.7% (37 of 59), and accuracy to 78.4% (87 of 111).

By applying the best cutoff point for each image, we found that elastography had a higher sensitivity than conventional US ($P < .05$). Elastography had lower specificity and lower accuracy than conventional US, but these differences were not significant. Therefore, when we considered the equivalence band, the specificity of elastography was not inferior to (ie, not more than 15% different than) ($P < .05$) and accuracy was equivalent to (ie, within 13% of) ($P < .05$) that of conventional US.

When the conventional US cutoff point was set between BI-RADS category 3 and 4, only two lesions had false-negative results, but 22 lesions had false-positive results. More than half of the false-positive lesions (14 [64%] of 22 lesions) had elasticity scores of 1 or 2 (score of 1, nine lesions; score of 2, five lesions). When the conventional US cutoff point was set between BI-RADS category 4 and 5, only two lesions had false-positive results, but 15 lesions had false-negative results. More than half of the false-negative lesions (11 [73%] of 15 lesions) had elasticity scores of 4 or 5 (score of 4, eight lesions; score of 5, three lesions).

In contrast, when the cutoff point for elastography was set between scores of 3 and 4, the majority of the false-negative results at elastography (six [86%] of seven lesions) were for lesions with a BI-RADS category of 4 or 5 (category 4, three lesions; category 5, three lesions); the one remaining lesion was classified as BI-RADS category 3. Of the six false-positive findings at elastography, three were for BI-RADS category 4 lesions, one was for a BI-RADS category 3 lesion, and two were for BI-RADS category 2 lesions.

In the first stage of the study, the sensitivity, specificity, and accuracy of elastography were 89.3% (25 of 28), 93.1% (27 of 29), and 91.2% (52 of 57), respectively, with a cutoff point of between 3 and 4. Also in the first stage of the study, the sensitivity, specificity, and accuracy of conventional US were 78.6% (22 of 28), 93.1% (27 of 29), and 86.0% (49 of 57), respectively, with a cutoff point of between 4 and 5.

In the second stage of the study, the sensitivity, specificity, and accuracy of elastography were 83.3% (20 of 24), 86.7% (26 of 30), and 85.2% (46 of 54), respectively, with a cutoff point of between 3 and 4. For conventional US, the sensitivity, specificity, and accuracy were 62.5% (15 of 24), 100% (30 of 30), and 83.3% (45 of 54), respectively, with a cutoff point of between 4 and 5. There was no significant difference between the first and second stage of the study with respect to the sensitivity, specificity, and accuracy of elastography and conventional US ($P > .05$). Therefore, we combined results for the two stages of subsequent analyses.

Table 4

Sensitivity, Specificity, and Accuracy of Elastography and Conventional US at Various Cutoff Points for the Diagnosis of Benign and Malignant Lesions

Cutoff Point*	Sensitivity (%)	Specificity (%)	Accuracy (%)
Elasticity score			
Between 1 and 2	100 (52/52)	35.6 (21/59)	65.8 (73/111)
Between 2 and 3	90.4 (47/52)	67.8 (40/59)	78.4 (87/111)
Between 3 and 4	86.5 (45/52)	89.8 (53/59)	88.3 (98/111)
Between 4 and 5	48.1 (25/52)	98.3 (58/59)	74.8 (83/111)
Conventional US category†			
Between 1 and 2	100 (52/52)	0 (0/59)	46.8 (52/111)
Between 2 and 3	100 (52/52)	23.7 (14/59)	59.5 (66/111)
Between 3 and 4	96.2 (50/52)	62.7 (37/59)	78.4 (87/111)
Between 4 and 5	71.2 (37/52)	96.6 (57/59)	84.7 (94/111)

Note.—Numbers in parentheses were used to calculate percentages.

* Cutoff points are presented for the entire study period (ie, for stage one and stage two).

† Conventional US category was defined according to the BI-RADS classification for US.

Discussion

Investigators have performed freehand US elastography in patients with breast lesions by using off-line assessment and have compared the traced outlines of tumors on B-mode images with those on grayscale elastograms (11,12). Although our method is similar to theirs, we were able to make an elasticity assessment instantly because our scoring system was simple; as a result, we believe our system is more practical for clinical use. A freehand US elastography system that permits real-time assessment has been developed and clinically tested. The freehand system uses spatial correlation and has rapid signal processing (12); however, the CAM provides a higher frame rate while maintaining high image quality. The other system uses a one-dimensional search; as a result, the performance of this sys-

tem can be compromised by lateral movement of the probe (11).

From a diagnostic point of view, our findings concur with those of other studies—namely, that elastography is useful for characterizing breast lesions in general and has the potential to allow differentiation between malignant and benign lesions (1,11–13). In the clinical setting, grayscale US elastography during which patients are imaged in a seated position has been performed for those with breast lesions, and motor-driven compression plates have been used (1). Investigators have reported that elastography allowed differentiation of cancers from fibroadenomas, and that the width of the cancers was greater on elasticity images than on B-mode images. Our results, which are derived with the more clinically practical freehand approach, correspond with theirs. In addition, we believe that our system is more rapid for demonstrating longitudinal displacement and more robust for lateral movement of the probe. With our system, lesions can be easily found because translucent color-scale elasticity images are superimposed on the corresponding B-mode images.

Clinical Implications

Although we are not yet able to precisely quantitate elasticity, we have arrived at a point where semiquantitative assessment in the clinical setting is possible.

Our finding of a significant difference between mean elasticity scores for malignant and benign lesions in patients suggests that elastography may be useful in diagnosing breast lesions in the clinical setting. Moreover, this discriminatory capability did not depend on lesion size when lesions were smaller than 30 mm in diameter. The mean elasticity score for scirrhous carcinoma was significantly higher than that for DCIS, and the mean scores for fibroadenoma and ANDI were lower than those for carcinomas. These results agree with experimental results for elastic moduli, as measured in vitro (14).

We believe that an elasticity score of 5, which shows no strain in the entire hypoechoic lesion and the surrounding area at B-mode US, indicates infiltration of cancer cells into the interstitial tissues (eg, in scirrhous carcinomas) or into an intraductal component (eg, in DCIS), both of which are characteristics of carcinoma.

An elasticity score of 4, which indicates no strain in the entire hypoechoic lesion, seems to be characteristic of tumors such as solid tubular carcinomas that are circumscribed and homogeneously harder than the adjacent normal breast tissue.

In our study, an elasticity score of 3, which indicates strain at the periphery of the hypoechoic lesion, was mainly found in benign lesions, including intraductal papillomas. The importance of strain at the periphery is unclear at present and requires further investigation. We recommend that all lesions with elasticity scores of 3 or higher be examined by means of aspiration cytology or needle biopsy because two (13%) of the 15 lesions with a score of 3 were malignant.

We believe that elasticity scores of 2, for which parts of the hypoechoic lesion did not show strain at B-mode US, indicate lesions that are soft yet somewhat harder than normal breast tissue. This is often characteristic of lesions such as fibroadenoma or ANDI. Of the five malignant lesions with scores of 2, two were DCIS and three were invasive ductal carcinomas at histologic analysis. Investigators have noted that DCIS is softer than invasive ductal carcinoma (14). The finding of a lower elasticity score in lesions suspicious for DCIS is therefore plausible and suggests that correct diagnosis of these lesions will require the use of other imaging modalities in addition to elastography.

Three patients with invasive ductal carcinoma had lesions with a score of 2, but we found no specific histologic features to explain the lower elasticity score in these patients. These false-negative results may have resulted from an artifact that was created by applying the probe with too much pressure during elastography. Two of these lesions were examined in the first stage of our study, and the examiner did not grasp the probe with an appropriate level of pressure. All of the invasive ductal carcinomas with a score of 2 (three lesions) were classified as BI-RADS category 4 or 5, a finding that supports the combined use of elastography and conventional US to avoid misdiagnosing an invasive carcinoma as a benign lesion.

We believe that an elasticity score of 1, which shows even strain in the entire hypoechoic lesion at B-mode US, indicates that lesions have almost the same compressibility as the surrounding breast tissue. In our study, no malignant lesions had a score of 1. Although our findings will require confirmation, this result suggests that invasive diagnostic procedures, such as histologic examination, may be omitted for patients who have lesions with a score of 1.

The result of our receiver operating characteristic curve analysis suggests that elastography may have a diagnostic performance that is better than, or at least equal to, that of conventional US, with the best cutoff point in the means of high sensitivity. Both accuracies coincide with each other within a 13% difference, and the specificity of elastography was not inferior to (ie, not more than 15% different than) that of conventional US. These results show that, compared with conventional US, elastography has higher sensitivity, a noninferior specificity of no more than 15%, and an equivalent accuracy of within 13%, which encourages us to believe that the results were obtained with elastography only. Because classifying elasticity images with our scoring system is simpler than classifying images with a scoring system based on the BI-RADS criteria for conventional US, we believe that even an examiner with limited training may be able to obtain the same diagnostic performance as an experienced examiner with elastography.

Of particular note, 14 (64%) of 22 patients who had false-positive results and a conventional US cutoff point of between BI-RADS category 3 and 4 had elasticity scores of 1 or 2; at minimum, the nine patients with a score of 1 could have conceivably been spared further procedures. In addition, we believe that, with concomitant use of elastogra-

phy and conventional US, it may be possible to downgrade some BI-RADS category 3 and 4 lesions to BI-RADS category 2 lesions. As a result, this approach may reduce the number of false-positive results and unnecessary invasive diagnostic procedures.

Limitations

Our study has some limitations. Patients with cancer were overrepresented because our hospital serves as a referral center for general clinics. Therefore, the findings cannot necessarily be extended to the general population. In addition, the lesions that were assessed were predominantly larger lesions. Although elastography facilitated the differentiation of malignant lesions from benign lesions (even among lesions smaller than 10 mm), few lesions in this study were smaller than 5 mm. Therefore, further studies on the use of elastography for the characterization of small lesions will be necessary.

Elastography itself, like all imaging modalities, has certain limitations. The main pitfall of this modality is that the extent of tissue compression influences both the elasticity image and, consequently, the elasticity score. When elasticity scores are used for diagnosis, images obtained with the application of strong pressure may lead to misdiagnosis. Images with minimal perturbation of strain relationships can be obtained by lightly pressing the probe to the breast. It takes some practice to be able to exert light pressure on the same cross-sectional surface of the breast. Of note, three (60%) of five false-negative results obtained by using an elasticity score cutoff point of between 3 and 4 occurred during the first stage of our study when the examiner was just getting used to the probe operation. We cannot, however, determine if the pressure was inappropriate because there is currently no pressure indicator available. Until a pressure gauge becomes available, examiners must attempt to apply the probe with light pressure by monitoring the real-time image to obtain images that are appropriate for elasticity analysis. Another shortcoming is that, although most images clearly resemble one of the five distinct patterns used for classification, the selection is currently made by the examiner and is not yet automated.

In conclusion, we believe that elastography can complement conventional US, thereby making it easier to diagnose breast lesions. Our experience suggests that the skill needed to acquire adequate images is similar for conventional US and elastography; the skill needed to interpret images, however, is somewhat less for elastography when our classification system is used. Elastography is promising, and we expect that with future improvements in the technology (eg, the development of a pressure indicator and approaches for quantitative assessment), this imaging modality will become an invaluable tool for the diagnosis of breast diseases in the clinical setting.

Acknowledgment: We thank Susan London, MS, Biomedical Writing and Editing, Seattle, for the correction of our manuscript.

References

1. Garra BS, Cespedes EI, Ophir J, et al. Elastography of breast lesions: initial clinical results. Radiology 1997;202:79–86.
2. Shiina T, Doyley MM, Bamber JC. Strain imaging using combined RF and envelope autocorrelation processing. In: Proceedings of the IEEE Ultrasonics Symposium. Savoy, Ill: Institute of Electrical and Electronics Engineers Ultrasonics, Ferroelectrics, and Frequency Control Digital Archive, 1996;2: 1331–1336.
3. Shiina T, Nitta N, Ueno E, Bamber JC. Real time tissue elasticity imaging using the combined autocorrelation method. J Med Ultrason 2002;29:119–128.
4. Nitta N, Yamakawa M, Shiina T, Ueno E, Doyley MM, Bamber JC. Tissue elasticity imaging based on combined autocorrelation method and 3-D tissue model. In: Proceedings of the IEEE Ultrasonics Symposium. Savoy, Ill: Institute of Electrical and Electronics Engineers Ultrasonics, Ferroelectrics, and Frequency Control Digital Archive, 1998;2: 1447–1450.
5. Yamakawa M, Shiina T. Strain estimation using the extended combined autocorrelation method. Jpn J Appl Phys 2001;40:3872–3876.
6. American College of Radiology. Breast imaging reporting and data system (BI-RADS), ultrasound. 4th ed. Reston, Va: American College of Radiology, 2003. Available at: http://www.acr.org/s_acr/sec.asp?CID=882&DID=14550. Accessed September 8, 2004.
7. Japanese Breast Cancer Society. General rules for clinical and pathological recording of breast cancer. 15th ed. Tokyo, Japan: Japanese Breast Cancer Society, 2002.
8. Hughes LE. The ANDI concept and classification of benign breast disorders: an update. Br J Clin Pract Suppl 1989;68:1–6.
9. Matsumura T, Tamano S, Mitake T, et al. Development of freehand ultrasound elasticity imaging system and in vivo results. In: Proceeding of the 1st International Conference on the Ultrasonic Measurement and Imaging of Tissue Elasticity. Rochester, NY: University of Rochester, 2002;1:80.
10. Tango T. Equivalence test and confidence interval for the difference in proportions for the paired-sample design. Stat Med 1998; 17(8):891–908.
11. Hiltawsky KM, Kruger M, Starke C, et al. Freehand ultrasound elastography of breast lesions: clinical results. Ultrasound Med Biol 2001;27:1461–1469.
12. Hall TJ, Zhu Y, Spalding CS. In vivo real-time freehand palpation imaging. Ultrasound Med Biol 2003;29:427–435.
13. Krouskop TA, Younes PS, Srinivasan S, Wheeler T, Ophir J. Differences in the compressive stress-strain response of infiltrating ductal carcinomas with and without lobular features: implications for mammography and elastography. Ultrason Imaging 2003;25: 162–170.
14. Krouskop TA, Wheeler TM, Kallel F, Garra BS, Hall T. Elastic moduli of breast and prostate tissue under compression. Ultrason Imaging 1998;20:260–274.

Japanese Journal of Applied Physics
Vol. 45, No. 5B, 2006, pp. 4740–4748

Pressure Gradient Estimation Based on Ultrasonic Blood Flow Measurement

Naotaka NITTA*, Kazuhiro HOMMA and Tsuyoshi SHIINA[1]

Institute for Human Science and Biomedical Engineering, National Institute of Advanced Industrial Science and Technology (AIST), 1-2-1 Namiki, Tsukuba, Ibaraki 305-8564, Japan
[1]*Graduate School of Systems and Information Engineering, University of Tsukuba, 1-1-1 Tennoudai, Tsukuba, Ibaraki 305-8573, Japan*

(Received November 30, 2005; revised February 26, 2006; accepted March 1, 2006; published online May 25, 2006)

Mechanical load to the blood vessel wall, such as shear stress and pressure, which occurs in blood flow dynamics, contribute greatly to plaque rupture in arteriosclerosis and to biochemical activation of endothelial cells. Therefore, noninvasive estimations of these mechanical loads are able to provide useful information for the prevention of vascular diseases. Although the pressure is the dominant component of mechanical load, for practical purposes, the pressure gradient is also often important. So far, we have investigated the estimation of the kinematic viscosity coefficient using a combination of the Navier-Stokes equations and ultrasonic velocity measurement. In this paper, a method for pressure gradient estimation using the estimated kinematic viscosity coefficient is proposed. The validity of the proposed method was investigated on the basis of the analysis with the data obtained by computer simulation and a flow phantom experiment. These results revealed that the proposed method can provide a valid estimation of the pressure gradient. [DOI: 10.1143/JJAP.45.4740]

KEYWORDS: vessel wall, mechanical loads, blood velocity measurement, kinematic viscosity coefficient, pressure gradient

1. Introduction

Mechanical load to the blood vessel wall, such as shear stress and pressure, which occurs in blood flow dynamics, contribute greatly to plaque rupture in arteriosclerosis and to biochemical activation of endothelial cells.[1–7] Therefore, noninvasive estimations of these mechanical loads are able to provide useful information for the prevention of vascular diseases.

Mechanical load to the blood vessel wall as a result of blood flow is roughly classified by the tangential force and the force normal to the vessel wall. Here, the tangential and normal forces correspond to shear stress and pressure, respectively. Pressure is the dominant component in mechanical load because its magnitude is much larger than that of shear stress. On the other hand, for practical purposes, the pressure gradient is often more important than the pressure itself. For example, the pressure loss produced at the stenosed part due to arteriosclerosis plaque is frequently calculated using the Doppler velocity measurement and the simplified Bernoulli equation. Since the pressure loss is defined by the differential pressure between two points, the pressure loss corresponds to the pressure gradient, which is the spatial gradient of the pressure distribution. Therefore, the pressure gradient calculation of the blood flow is important and useful when analyzing the blood flow dynamics.

We have investigated a method for estimating the kinematic viscosity coefficient of fluid using a combination of the Navier-Stokes equations and ultrasonic velocity vector measurement.[8] Moreover, a method for assessing the intravascular shear stress has also been investigated on the basis of the estimated kinematic viscosity coefficient under the assumption of a known density.[9] In addition, an assessment with respect to pressure is necessary for completing the hemodynamics analysis.

The conventional method for estimating the pressure gradient is based on the Stokes equation, assuming unidirectional flow, and the application of the least-squares method to all velocity data within the flow field.[10] Therefore, it is difficult to obtain the intravascular distribution of the pressure gradient.

In this study, by extending the previous method for estimating the kinematic viscosity coefficient, a method for estimating the pressure gradient and its distribution is developed, without the assumption of unidirectional flow, on the basis of a combination of the Navier-Stokes equations and the ultrasonic velocity vector field. The validity of this method is investigated by using analyzing data obtained by computer simulation and a flow phantom experiment.

This paper is structed as follows. In §2, a method for estimating the pressure gradient on the basis of the kinematic viscosity coefficient estimation is proposed. In §3 and §4, the analysis results of the data obtained by simulation and experiment are presented. In §5, we discuss the conclusions.

2. Principle of Pressure Gradient Estimation

It is assumed that blood is an isotropic and incompressible viscous fluid and that the velocity vector distribution has already been obtained in the palmic phase in which Newtonian properties can be assumed.

Here, in view of practicality, a two-dimensional (2D) flow state is treated. More detailed theory of the three-dimensional (3D) flow state is discussed in the appendix. In the 2D flow state, the pressure gradient components in the Cartesian coordinate system can be described, on the basis of the Navier-Stokes equations, as follows:

$$\frac{\partial p}{\partial x} = \rho(\nu X - U), \tag{1}$$

$$\frac{\partial p}{\partial y} = \rho(\nu Y - V), \tag{2}$$

where ρ and ν are the density and the kinematic viscosity coefficient, respectively. U, V, X, and Y are defned only by velocity vector components, (u, v), as

$$U = \frac{\partial u}{\partial t} + u\frac{\partial u}{\partial x} + v\frac{\partial u}{\partial y}, \tag{3}$$

$$V = \frac{\partial v}{\partial t} + u\frac{\partial v}{\partial x} + v\frac{\partial v}{\partial y}, \tag{4}$$

*E-mail address: n.nitta@aist.go.jp

$$X = \frac{\partial^2 u}{\partial x^2} + \frac{\partial^2 u}{\partial y^2}, \tag{5}$$

$$Y = \frac{\partial^2 v}{\partial x^2} + \frac{\partial^2 v}{\partial y^2}. \tag{6}$$

On the other hand, the kinematic viscosity coefficient ν can be derived, by eliminating the pressure terms in eqs. (1) and (2), as[8]

$$\nu = \frac{\dfrac{\partial \xi}{\partial t} + u\dfrac{\partial \xi}{\partial x} + v\dfrac{\partial \xi}{\partial y}}{\dfrac{\partial^2 \xi}{\partial x^2} + \dfrac{\partial^2 \xi}{\partial y^2}}, \tag{7}$$

where ξ is the vorticity defined as

$$\xi = \frac{\partial v}{\partial x} - \frac{\partial u}{\partial y}. \tag{8}$$

Since we assume an incompressible fluid, there is no spatial gradient of the density, and the density is constant in the flow field. Therefore, by assuming a known density, the pressure gradients can be obtained by substituting the kinematic viscosity coefficient of eq. (7) into eqs. (1) and (2). This means that the pressure gradients can be obtained from only the velocity vector distribution.

Although a 2D velocity vector distribution is necessary for obtaining the pressure gradients, only one velocity component along the beam axis can be measured by the present ultrasonic Doppler method. In order to obtain the component orthogonal (lateral) to the beam axis, the incompressible condition can be adopted.[8] Therefore, a 2D velocity vector distribution can be composed by the measurement of the beam axis component by the ultrasonic Doppler method and the estimation of the lateral component under the incompressible condition.

On the other hand, $\nabla p = (\partial p/\partial x, \partial p/\partial y)$ means a vector in the Cartesian coordinate system because the pressure p is a scalar. This means that the pressure gradients vary according to the assignment of the Cartesian coordinate. In the ultrasonic measurement, the beam direction could be adopted as one axis in the Cartesian coordinate system. In other words, the pressure gradients vary according to the positioning of the ultrasonic probe. Therefore, for the independent assessment of probe positioning, it is promising to calculate the pressure gradient along the tangential direction of the streamline, which is the curve whose tangential vector corresponds to the velocity vector. Therefore, by transforming the coordinate system so that one of the directional vectors along the original Cartesian coordinate axes determined by probe positioning agrees with the velocity vector direction, the tangential pressure gradient of the streamline can be obtained. Since ∇p is a vector, the coordinate transformation due to rotation can be applied to obtain the tangential pressure gradient.

In the Cartesian coordinate system shown in Fig. 1, the pressure gradient vector $(\partial p/\partial x, \partial p/\partial y)$ in the O–xy system determined by probe positioning can be transformed to the vector $(\partial p/\partial x', \partial p/\partial y')$ in the O'–$x'y'$ system, as follows:

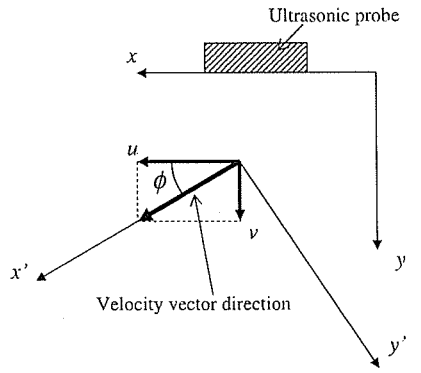

Fig. 1. Cartesian coordinate system determined by the position of the ultrasonic probe and its coordinate transformation by rotation.

$$\begin{pmatrix} \dfrac{\partial p}{\partial x'} \\ \dfrac{\partial p}{\partial y'} \end{pmatrix} = \begin{pmatrix} \cos\phi & \sin\phi \\ -\sin\phi & \cos\phi \end{pmatrix} \begin{pmatrix} \dfrac{\partial p}{\partial x} \\ \dfrac{\partial p}{\partial y} \end{pmatrix}. \tag{9}$$

In Fig. 1, since the coordinate system is transformed such that the x' axis agrees with the tangential direction of the streamline, the tangential pressure gradient can be obtained as

$$\frac{\partial p}{\partial x'} = \frac{\partial p}{\partial x}\cos\phi + \frac{\partial p}{\partial y}\sin\phi. \tag{10}$$

The rotation angle ϕ is obtained from the velocity vector. In Fig. 1, when the x' axis agrees with the velocity vector direction, the v' component along the y' axis becomes zero in the transformed O'–$x'y'$ system. Using this relationship, each component of the transformation matrix in eq. (9) can be denoted, with the velocity vector components, as

$$\cos\phi = \frac{u}{V}, \tag{11}$$

$$\sin\phi = \frac{v}{V}, \tag{12}$$

where V is the absolute value of the velocity vector and is defined by $V = \sqrt{u^2 + v^2}$. Finally, by substituting eqs. (11) and (12) into eq. (10), the tangential pressure gradient of the streamline can be derived as

$$\frac{\partial p}{\partial x'} = \frac{\partial p}{\partial x}\frac{u}{V} + \frac{\partial p}{\partial y}\frac{v}{V}. \tag{13}$$

This means that the tangential pressure gradient can be derived by using the pressure gradient vector and the velocity vector in the original coordinate system determined by the probe position, without cumbersome calculation concerning the rotation angle ϕ.

3. Simulation Analysis

The validity of the proposed method for estimating the pressure gradients was investigated by simulation analysis. As shown in Fig. 2, a 3D flow model with a step imitating the arteriosclerosis plaque structure, where the vorticity required for estimating the kinematic viscosity coefficient was arisen, was considered. The principle described in §2 involves a method based on the 2D velocity vector distribution from the viewpoint of practicality and this

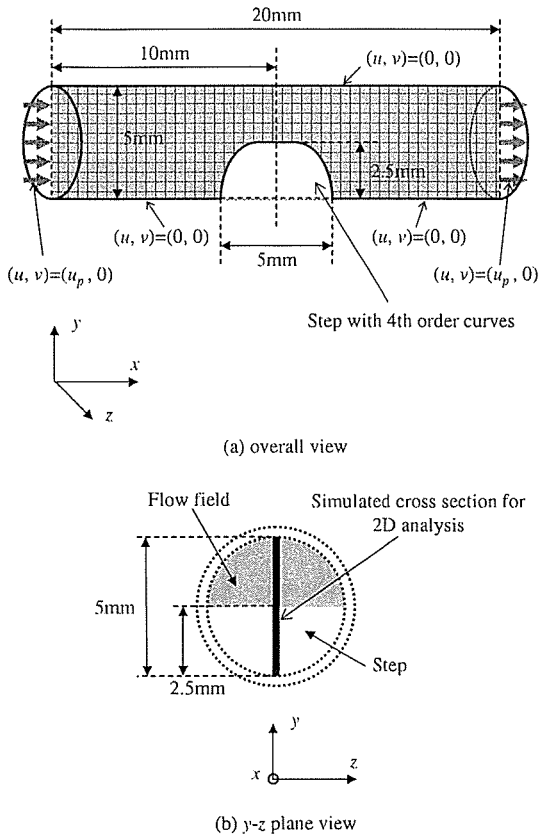

Fig. 2. Flow model for simulation. (a) Overall view of the model and (b) short-axis cross section of the tube on the y–z plane.

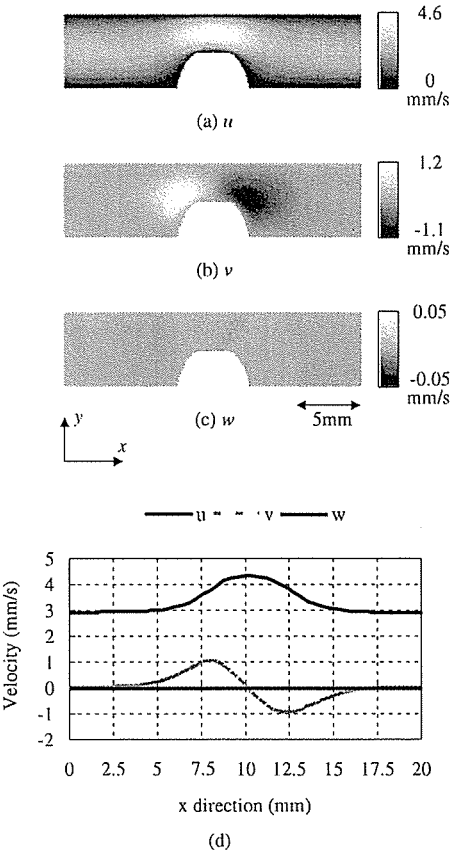

Fig. 3. Three-dimensional velocity vector components on the central cross section obtained by 3D finite element method. (a) x, (b) y, and (c) z components of the velocity vector distribution on the central cross section are shown, which are indicated as u, v, and w, respectively. (d) Vector component profiles of u, v and w on the central tube axis.

corresponds to the z component of the 3D velocity vector being neglected around the x–y cross section on the central tube axis shown in Fig. 2. Therefore, if the z component of the velocity vector on the x–y cross section is much smaller than the other components, it is expected that the actual pressure gradient on the same cross section can be estimated more accurately even if that estimation is based only on the 2D velocity vector.

In order to evaluate the magnitude of the z component on the x–y cross section, a 3D finite element method (FEM) was applied to the 3D flow model shown in Fig. 2. Although this model has a configuration similar to that of the previously investigated model,[8] the boundary conditions are different from the previous conditions. That is, the fixed boundary conditions at which the velocity vectors become 0 on the wall with the step, and the natural boundary conditions under which the velocity vectors are perpendicular to the faces at the inlet and the outlet of the model, are imposed. Navier–Stokes equations with a realistic kinematic viscosity coefficient (around $3.0\,\mathrm{mm^2/s}$) and density ($10^3\,\mathrm{kg/m^3}$) were solved by iterative FEM calculation, and the distributions of 3D velocity vector components on the cross section were obtained. A small initial value of the velocity component along the x axis was provided so that the iterative calculation would converge stably. The results are shown in Fig. 3 for (a) x, (b) y, and (c) z components of the velocity vector distribution on the cross section, where these components are indicated as u, v, and w, respectively. Figure 3(d) also shows the vector component profiles of u, v, and w on the central tube axis. As shown in Fig. 3, the total magnitude of w is much smaller than that of the other u and v distributions and is close to 0. The w distribution also exhibits an almost uniform pattern. This indicates that, for achieving more accurate estimation based on the 2D velocity vector alone, it is appropriate to use the 2D velocity vector distribution obtained on the central cross section in this tube structure. In order to avoid the huge computation time of the 3D FEM, in the following analysis, the 2D flow field analysis, in which the z component of the velocity vector is neglected, can be effectively performed by the finite difference method, based on the above findings of the 3D analysis. The 2D flow field analysis was performed on the x–y cross section, as shown in the dark area of Fig. 2, and the 2D velocity vector distributions were obtained. Here, the same boundary conditions as in the above 3D analysis were also used. In the following simulation, assuming that the 2D velocity vector distributions have already been obtained by ultrasonic measurements, the pressure gradients were estimated using the 2D velocity vector distributions obtained by this finite difference method.

Figure 4 shows the analysis results obtained with the kinematic viscosity coefficient of $3.0\,\mathrm{mm^2/s}$, where (a) and (b) display the streamline and the vorticity distributions, respectively. In the streamline, a valid distribution can be attained along the boundary configurations. In the vorticity

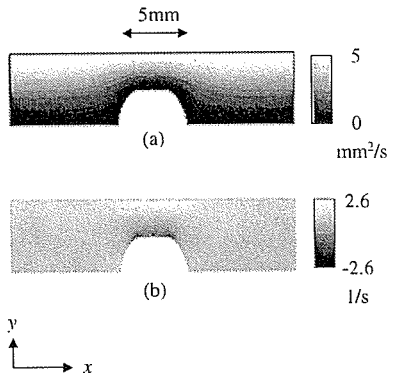

Fig. 4. (a) Streamline and (b) vorticity distributions obtained by the finite difference method.

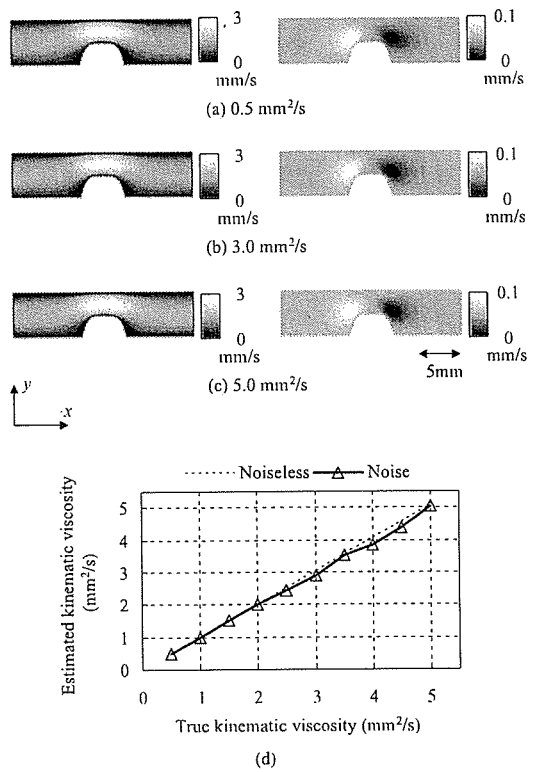

Fig. 5. Velocity vector distributions corresponding to the kinematic viscosity changes and the estimated result of the kinematic viscosity coefficient. In (a) to (c), left panels indicate the x-component distributions of the velocity vector (u), and right panels indicate the y-component distributions of the velocity vector (v). Each component of the velocity vector was obtained on the basis of the original Cartesian coordinate system. (d) True and the estimated values of the kinematic viscosity coefficients. Horizontal axis indicates the true values and the vertical axis indicates the estimated values.

distribution, it can be observed that the vorticity rises around the step.

Figure 5 shows the velocity vector distributions with the kinematic viscosity coefficients changed from 0.5 to 5.0 mm^2/s, and the results of the kinematic viscosity coefficients estimated using the velocity vector distributions. The broken line indicates the estimated result when the ideal velocity vector distributions without noise were utilized, and

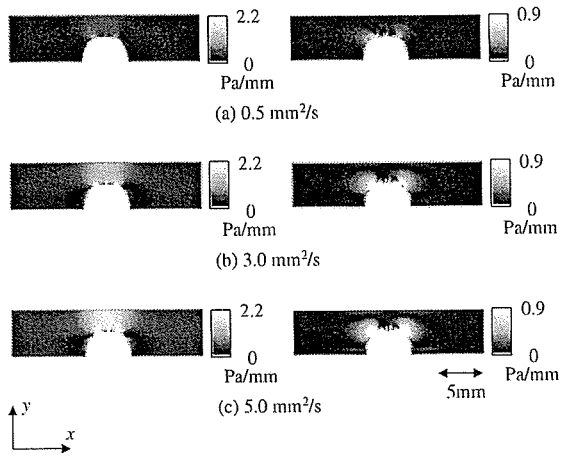

Fig. 6. Ideal pressure gradient distributions obtained using the velocity vector distributions without noise, corresponding to kinematic viscosity changes. In (a) to (c), left panels indicate the x-component distributions of the pressure gradient ($\partial p/\partial x$), and right panels indicate the y-component distributions of the pressure gradient ($\partial p/\partial y$). Each component of the pressure gradient was obtained on the basis of the original Cartesian coordinate system.

the solid line indicates the estimated result when the velocity vector distributions with white noise, which simulate those obtained by ultrasonic measurement, were utilized. Here, the amplitude of white noise was set to 40 dB lower than the maximum absolute value of the ideal velocity vector, and this white noise was added to each ideal velocity vector component. Similarly to the previous results,[8] valid kinematic viscosity estimations could be obtained.

Figure 6 shows the ideal pressure gradient distributions obtained using the velocity vector distributions without noise when the kinematic viscosity coefficients were changed from 0.5 to 5.0 mm^2/s. Since the velocity vector data were obtained on the square grids in this simulation, the difference width was set to 0.2 mm along both x and y directions in calculating eqs. (3) to (6) by the central difference method, and the pressure gradient distribution was attained. Each component of the pressure gradient obtained on the basis of the original Cartesian coordinate system is displayed. In this case, the pressure gradients become larger according to the kinematic viscosity increase. Also, it can be observed that the pressure gradients around the step are larger than those in other regions.

Figure 7 shows the tangential pressure gradient $\partial p/\partial x'$ distributions estimated using the velocity vector distributions and the pressure gradients, $\partial p/\partial x$ and $\partial p/\partial y$, when the kinematic viscosity coefficients were changed from 0.5 to 5.0 mm^2/s. These results show the pressure gradient acting along the streamlines shown in Fig. 4(a). Left panels indicate the ideal tangential pressure gradient obtained using the ideal velocity vector distributions without noise and the true kinematic viscosity coefficient, and right panels indicate the estimated tangential pressure gradient obtained using the velocity vector distributions with the same white noise as that in the case of Fig. 5 and the estimated kinematic viscosity coefficient. Dynamic ranges in all images are standardized. Estimated distributions coincide well with the ideal distributions. Figure 7(d) shows the comparison be-

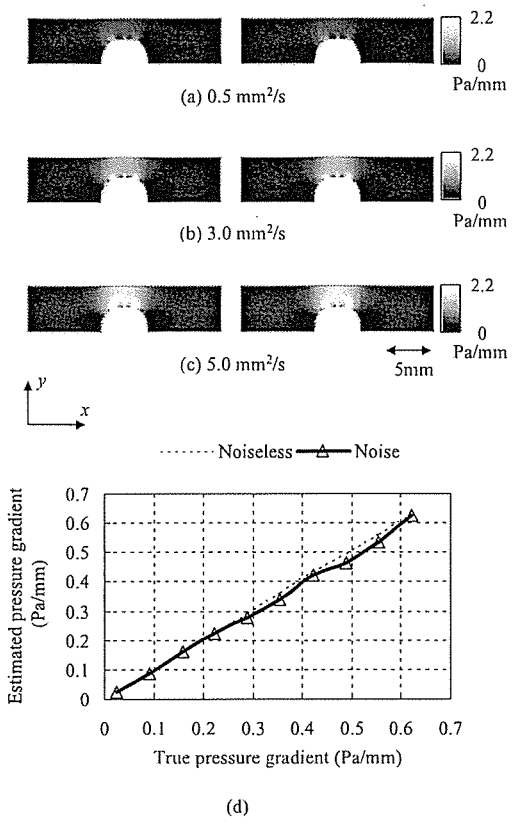

(d)

Fig. 7. Tangential pressure gradient estimation along the streamline. In (a) to (c), left panels indicate the ideal tangential pressure gradients obtained using the velocity vector distributions without noise, and right panels indicate the estimated tangential pressure gradients obtained using the velocity vector distributions with noise. (d) True and estimated values of the tangentinal pressure gradients. Horizontal axis indicates the true values and the vertical axis indicates the estimated pressure gradient values.

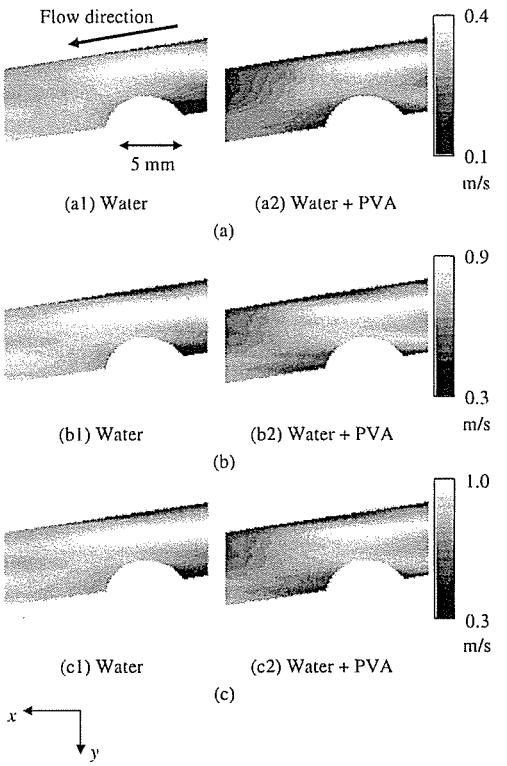

Fig. 8. Results of 2D velocity vector measurements. Left panels show the results for water and right panels show the results for water mixed with PVA. (a) Beam axis component. (b) Estimated lateral component. (c) Absolute values of velocity vector. Maximum and minimum values of each vector component along the axes on the *xy* coordinate system are assigned as white and black pixels, respectively.

tween the ideal (true) and the estimated tangential pressure gradients. The horizontal axis indicates the true values and the vertical axis indicates the estimated pressure gradient values. Here, the broken line indicates the estimated result when the ideal velocity vector distributions without noise were applied, and the solid line indicates the estimated result when the velocity vector distributions with noise were applied. This figure also shows that the estimated values coincide well with the true values. From these results, it was confirmed that the proposed method can be used to estimate a valid tangential pressure gradient when the velocity vector distributions can be accurately obtained.

4. Experimental Data Analysis

To verify the validity of the proposed method empirically, data obtained in a flow phantom experiment were analyzed. In the experiment, the same setup as that in a previous work[8] was applied. Here, a brief explanation of the setup is described.

Similar to the simulation analysis, a step imitating the plaque structure was placed on the inner wall of a silicone tube with a diameter of 5 mm, to generate the velocity vector field. Two fluid types, water and water mixed with poly(vinyl alcohol) (PVA), were prepared. The kinematic viscosity coefficient increases upon mixing PVA with water. As a result of the measurement with a viscometer, the kinematic viscosity coefficients of water and water mixed with PVA were found to be 1.5 and 6.2 mm^2/s, respectively, at the temperature of 21 °C. Rice powder was mixed into each type of fluid to cause the ultrasonic scattering. These fluids flowed through the tube at a speed of 1.0 m/s as a steady flow, and the temperature of fluids was kept at 21 °C. The tube was placed in a water tank, and the ultrasonic probe for measuring the velocity was set at the top of the tube at a distance of 50 mm from the center axis of the tube. The angle between the central tube axis and the ultrasonic beam direction was set to 67°.

The ultrasonic probe was driven at a center frequency of 4.7 MHz. The beam axis velocity profile was measured by the autocorrelation method in the Doppler method, using the echo train data obtained by transmitting 74 pulses in the same direction. The beam axis velocity distribution, which is composed by 20 scan lines, was obtained by scanning the probe horizontally with the stepping motor drive.

Lateral velocity component, which is orthogonal to the beam axis component, was obtained by applying a method utilizing the incompressible condition, as in the previous work.[8]

The 2D velocity vector distributions on the central cross section of the tube, obtained by the above-described process, are shown in Fig. 8 for (a) the beam axis component, (b) the estimated lateral component and (c) the absolute values of the velocity vector. Left panels show the results for water

and right panels show the results for water mixed with PVA. The kinematic viscosity coefficient is estimated using these velocity vector distributions, and furthermore, the mutually perpendicular pressure gradients determined by probe positioning are estimated; ultimately, the tangential pressure gradient distribution acting along the streamline is obtained. As a results of the kinematic viscosity estimated using the 2D velocity vector distributions shown in Fig. 8, the kinematic viscosity coefficients of water and water mixed with PVA were found to be 1.25 and 6.24 mm^2/s, respectively. These estimated values are close to the values measured with the viscometer, indicating valid results. Although the estimation for higher viscosity fluid exhibits higher accuracy than for lower viscosity fluid when comparing the ultrasonic estimations with the kinematic viscosity values measured with the viscometer, we believe that this accuracy is not universal. In this experiment, the accuracies of the velocity vector measurement for these two fluids are the same because these fluids flow in the tube at the same speed. Although there locally exist regions of lower velocity and the flow pattern becomes complex in the higher viscosity fluid, it is predicted that the same accuracies can be obtained for the kinematic viscosity estimation because all flow speeds are the same and the kinematic viscosity coefficient is calculated as an average around the stenosis. As the reason behind the occurrence of the difference between the estimation accuracies, various factors, such as a statistically insufficient number of experimental data and viscosity fluctuations due to the minute variations of the fluid temperature, might be given. Although the statistical tendency of the kinematic viscosity estimation must be assessed in the future, it can at least be considered that a valid estimation was accomplished in this study, because the kinematic viscosity estimation can be performed with good accuracy and the two fluids can be discriminated on the basis of the estimated kinematic viscosity coefficients.

When the central difference method is directly applied to the velocity vector distribution including fluctuation due to noise, as shown in Fig. 8, the accuracy of the pressure gradient distribution decreases because the noise is amplified due to the high-order derivative term calculation. In order to suppress the errors due to difference operation and to stabilize the calculations of the pressure gradient distribution, each distribution of the velocity vector components was interpolated by the polynomial approximation technique and differentiated by the central difference method. When applying the polynomial approximation, it is important to determine its order. In this study, different orders were used when each velocity component distribution was approximated by the polynomial approximation along x and y directions, because these velocity profiles along the x and y directions are different from each other.

First, the y direction almost corresponds to the radial direction of the tube, because of the tube placement. If the flow is laminar, the velocity profile along the radial direction becomes a parabolic curve. Consequently, u and v profiles along the y direction can also be approximated as a parabolic curve. In this experiment, although the tube does not have a uniform diameter because it includes the step, if the conditions for laminar flow are satisfied, the velocity profile along the y direction can also be approximated as a parabolic curve. Therefore, the conditions for laminar flow in this experiment were evaluated using the Reynolds number, which is defined as $U_m D/\nu$, where U_m, D, and ν are the mean velocity, the tube diameter, and the kinematic viscosity coefficient, respectively. Since this tube structure is divided into the stenosed part and the non-stenosed part, Reynolds numbers at each part for water and water mixed with PVA were calculated by substituting the values of the measured mean velocity, the diameter at each part and the kinematic viscosity coefficient measured with the viscometer into the definition of the Reynolds number. As a consequence, the Reynolds numbers were 1666 at the non-stenosed part and 2000 at the stenosed part in water, and 403 at the non-stenosed part and 483 at the stenosed part in water mixed with PVA. In general, since the critical Reynolds number is about 2000 in the tube,[11] the flow patterns in this experiment can be roughly approximated as a laminar flow. Therefore, the order of the polynomial approximation along the y direction was set to be 2, because it is expected that the velocity profile along the y direction would be close to a parabolic curve.

The order of the polynomial approximation along the x direction is determined to reduce the difference between the polynomial approximation and the actual measured distributions because there is no *a priori* information such as the parabolic curve. In order to determine this order, the polynomial approximations were performed changing the orders up to 7, and the errors were evaluated, as shown in Fig. 9. Naturally, although the higher order causes the approximation accuracy to increase, error updating in all curves shown in Fig. 9 almost reaches a plateau above the 5th order. This result indicates that 5th or higher order polynomial approximation along the x direction is valid for these experimental data. In order to achieve more accurate approximation, 7th-order polynomial approximation was used for the interpolation along the x direction. For the above determination of the order and the polynomial approximation, the interpolated 2D velocity vector distributions are shown in Fig. 10. On the whole, although the velocity distributions shown in Fig. 8 are smoothed by the

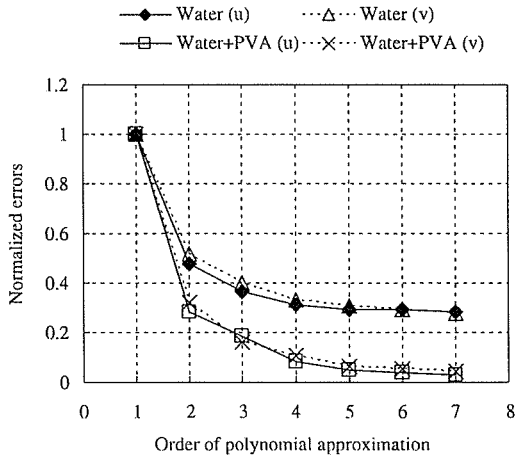

Fig. 9. Relationship between the orders of polynomial approximation and the normalized errors of the polynomial approximation along x directions for u and v distributions in water and water mixed with PVA.

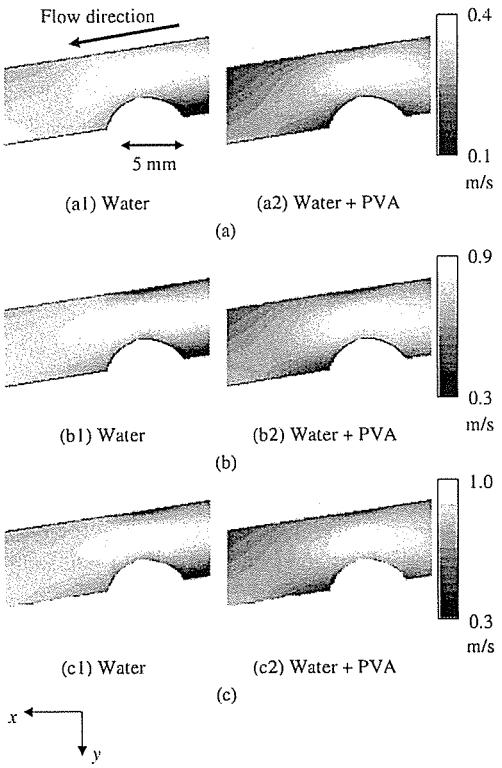

Fig. 10. Incorpolated 2D velocity vector distributions by the polynomial approximation method. Seven orders of polynomial approximation were set for the lateral direction and 2 orders for the beam-axis direction. Left panels show the results for water and right panels show the results for water mixed with PVA. (a) Beam axis component. (b) Estimated lateral component. (c) Absolute values of the velocity vector. Maximum and minimum values of each vector component along the axes on the xy coordinate system are assigned as white and black pixels, respectively.

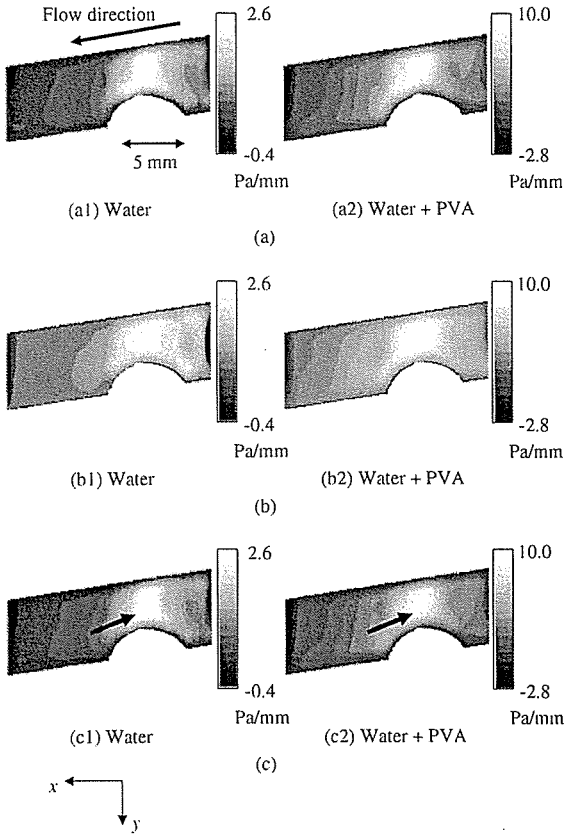

Fig. 11. Results of the pressure gradient estimation based on the velocity vector distribution. Left panels show the results for water and right panels show the results for water mixed with PVA. (a) x and (b) y components of the pressure gradients on the xy coordinate system. (c) Estimated tangential pressure gradient along the streamline. In (a) and (b), maximum and minimum values of each gradient component along the axes on the xy coordinate system are assigned as white and black pixels. In (c), maximum and minimum values of the tangential pressure gradient along the streamline are assigned as white and black pixels.

polynomial approximation, Fig. 10 reflects the features in Fig. 8.

After interpolating the velocity vector distributions, the pressure gradient distributions were calculated by central difference operations with difference widths along the x and y directions set to 1 and 0.45 mm, respectively. Figure 11 shows the pressure gradient distribution obtained with the estimated kinematic viscosity coefficient and the velocity vector distribution. Left panels show the results for water and right panels show the results for water mixed with PVA. Figures 11(a) and 11(b) show the pressure gradient components obtained using eqs. (1) and (2), and these correspond to the x and y components of the pressure gradients on the xy coordinate system, respectively. However, these were governed by the probe position. That is, the x axis corresponds to the lateral direction, and the y axis corresponds to the beam axis direction. As mentioned in §2, the pressure gradient assessment based on probe position, that is, the angle between the beam and the flow axes, is not invariant. Figure 11(c) shows the estimated distribution of the tangential pressure gradient acting along the streamline. Similar to the simulation results, the valid result that the tangential pressure gradient around the step arrowed in Fig. 11(c) is larger than that in the other regions was observed. Thus, the tangential pressure gradient can be used to assess the property of the flow itself, independently of the probe position.

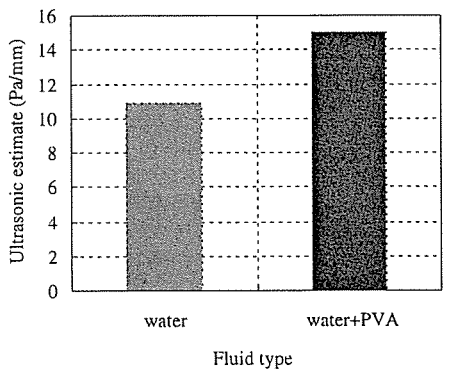

Fig. 12. Tangential pressure gradients around the step for the two types of fluid, water and water mixed with PVA. These were obtained as absolute values.

Figure 12 shows the averaged tangential pressure gradients around the step for the two fluids. These were obtained as absolute values. The average value for water mixed with PVA is slightly larger than that for water. Since the flow rate

was maintained almost constant, it is predicted that the pressure gradient is affected by the estimated kinematic viscosity coefficient, as in the simulation results. Therefore, these results indicate that the proposed method can be used to estimate a valid pressure gradient.

5. Conclusions

In this paper, with the aim of assessing the mechanical load applied to the vessel wall because of blood flow, a method for estimating the pressure gradient distribution was proposed. This method involves the previously reported method for estimating the kinematic viscosity coefficient.[8] The validity of the proposed method was investigated by analyzing the data obtained by computer simulation and the flow phantom experiment. The results indicated that the proposed method can be used to estimate a valid pressure gradient distribution.

In the future, it will be necessary to improve the robustness to noise when estimating the pressure gradient distribution, because this method is based only on velocity vector distributions. In particular, the robustness is an important factor in applications to the actual human blood flow state. In order to improve the robustness, it is promising to improve the velocity vector calculation and the derivative operation.

In addition to the above future work, simulations and experiments concerning various vascular situations, such as carotid bifurcation, will be conducted, and furthermore, the proposed method will be applied to in vivo experiments.

1) E. Falk, P. K. Shah and V. Fuster: Circulation **92** (1995) 657.
2) M. Luiza, C. Albuquerque and A. S. Flozak: Exp. Cell Res. **270** (2001) 223.
3) K. Nguyen, C. Patterson, M. Runge, S. Eskin and L. Mcintire: Proc. 1999 BMES/EMBS Conf., 1999, Vol. 1, p. 9.
4) Q. Yuchen and J. M. Tarbell: Proc. 1999 BMES/EMBS Conf., 1999, Vol. 1, p. 209.
5) J. Hanjoong and C. B. Yong: Proc. 2002 EMBS/BMES Conf., 2002, Vol. 1, p. 639.
6) M. F. Coughlin and G. W. Schmid-Schonbein: Proc. 2002 EMBS/BMES Conf., 2002, Vol. 1, p. 308.
7) S. Muller, V. Labrador, S. Legrand, X. Wang, D. Dumas and J. F. Stoltz: Proc. 1999 BMES/EMBS Conf., 1999, Vol. 2, p. 1340.
8) N. Nitta and K. Homma: Jpn. J. Appl. Phys. **44** (2005) 4602.
9) N. Nitta, K. Homma and T. Shiina: Proc. 2005 IEEE Ultrason. Symp., 2005, p. 520.
10) C. C-Bacrie: Proc. 1999 IEEE Ultrason. Symp., 1999, Vol. 2, p. 1489.
11) Y. C. Fung: *Biomechanics: Circulation* (Springer-Verlag, New York, 1996).

Appendix: Pressure Gradient Estimation in 3D Flow State

In the 3D flow state, the pressure gradient vector components in the Cartesian coordinate system can be derived, using the Navier-Stokes equations, as

$$\frac{\partial p}{\partial x} = \rho\left(\nu\nabla^2 u - \frac{Du}{Dt}\right), \tag{A·1}$$

$$\frac{\partial p}{\partial y} = \rho\left(\nu\nabla^2 v - \frac{Dv}{Dt}\right), \tag{A·2}$$

$$\frac{\partial p}{\partial z} = \rho\left(\nu\nabla^2 z - \frac{Dz}{Dt}\right), \tag{A·3}$$

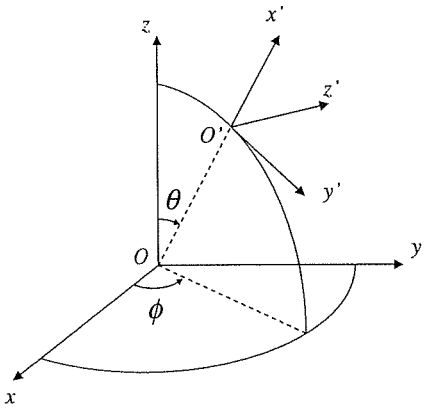

Fig. A·1. Coordinate transformation in a 3D space.

where ρ: density, ν: kinematic viscosity coefficient, u, v, w: velocity vector components, ∇^2: Laplacian, and D/Dt: Lagrangian operator.

Equations (A·1)–(A·3) indicate that the pressure gradient components can be obtained using only velocity vector components under the assumption of a known density, because the kinematic viscosity coefficient can be calculated when attaining the velocity vector.

However, the above pressure gradients depend on the assignment of the Cartesian coordinate system. Therefore, as an independent assessment of the assignment of the coordinate system, it is promising for the pressure gradient to be calculated along the tangential direction of the streamline.

In the Cartesian coordinate system shown in Fig. A·1, the pressure gradient vector $(\partial p/\partial x, \partial p/\partial y, \partial p/\partial z)$ in the original O–xyz system can be transformed to the vector $(\partial p/\partial x', \partial p/\partial y', \partial p/\partial z')$ in the O'–$x'y'z'$ system, as follows:

$$\begin{pmatrix} \frac{\partial p}{\partial x'} \\ \frac{\partial p}{\partial y'} \\ \frac{\partial p}{\partial z'} \end{pmatrix} = \begin{pmatrix} \sin\theta\cos\phi & \sin\theta\sin\phi & \cos\theta \\ \cos\theta\cos\phi & \cos\theta\sin\phi & -\sin\theta \\ -\sin\phi & \cos\phi & 0 \end{pmatrix} \begin{pmatrix} \frac{\partial p}{\partial x} \\ \frac{\partial p}{\partial y} \\ \frac{\partial p}{\partial z} \end{pmatrix}. \tag{A·4}$$

In Fig. A·1, since the coordinate system is transformed such that the x' axis agrees with the tangential direction of the streamline, the tangential pressure gradient can be obtained as follows:

$$\frac{\partial p}{\partial x'} = \frac{\partial p}{\partial x}\sin\theta\cos\phi + \frac{\partial p}{\partial y}\sin\theta\sin\phi + \frac{\partial p}{\partial z}\cos\theta. \tag{A·5}$$

The rotation angles ϕ and θ are obtained from the velocity vector. In Fig. A·1, when the x' axis agrees with the velocity vector direction, both the v' component along the y' axis and the w' component along the z' axis become zero in the transformed O'–$x'y'z'$ system. Applying this relationship, eq. (A·5) is reduced to eq. (A·6) using the velocity vector components.

$$\frac{\partial p}{\partial x'} = \frac{\partial p}{\partial x}\frac{u}{V} + \frac{\partial p}{\partial y}\frac{v}{V} + \frac{\partial p}{\partial z}\frac{w}{V}. \tag{A·6}$$

Here, V is the absolute value of the velocity vector and is defined by $V = \sqrt{u^2 + v^2 + w^2}$. This means that the tangential pressure gradient can also be derived using the pressure gradient vector and the velocity vector in the original coordinate system, without cumbersome calculations of the rotation angles ϕ and θ, even when the complex 3D flow state is considered.

Original Article

Association of Genetic Variation of the Adiponectin gene with Body Fat Distribution and Carotid Atherosclerosis in Japanese Obese Subjects

Yuko Katsuda[1], Akimichi Asano[1], Yuko Murase[1], Daisuke Chujo[1], Kunimasa Yagi[1], Junji Kobayashi[2], Hiroshi Mabuchi[2], and Masakazu Yamagishi[1]

[1]Molecular Genetics of Cardiovascular Disorders, Graduate School of Medical Science, Kanazawa University, Kanazawa, Japan.
[2]Department of Lipidology, Graduate School of Medical Science, Kanazawa University, Kanazawa, Japan.

Aim: The aim of this study was to investigate the effect of SNP45 of the adiponectin gene on body fat distribution and carotid atherosclerosis in Japanese obese subjects.
Methods: A total of 64 obese subjects were investigated. Genotypes of SNP45 were assayed by polymerase chain reaction-restriction fragment length polymorphism. Visceral fat area (VFA) and subcutaneous fat area (SFA) were measured using computed tomography. The progression of atherosclerosis was evaluated by plaque score (PS) of carotid artery using B-mode ultrasonography.
Results: Men carrying the G allele of SNP45 showed higher VFA (172.8 ± 50.8 vs. 147.1 ± 58.7, $p = 0.005$), lower SFA (209.9 ± 101.8 vs. 273.4 ± 142.2, $p = 0.007$), higher VFA/SFA (V/S) ratio (1.00 ± 0.46 vs. 0.60 ± 0.26, $p < 0.001$) and higher PS (9.5 ± 3.7 vs. 6.8 ± 4.2, $p = 0.012$) than those with TT genotype. Multivariate analysis showed that SNP45 was an independent determinant of V/S ratio and PS in men. In subgroup analysis, PS tended to be associated with V/S ratio only in the carrier of 45G allele.
Conclusion: These results suggest that the G allele could be a risk factor of metabolic syndrome and the development of atherosclerosis in Japanese obese subjects.

J Atheroscler Thromb, 2007; 14:19-26.

Key words; Visceral obesity, Plaque score, Polymorphism, PCR-RFLP

Introduction

Adiponectin is a 244-amino acid protein synthesized and secreted exclusively by adipose tissue[1, 2] and plays an important role in the regulation of energy homeostasis and insulin sensitivity[3-5]. Adiponectin also has anti-atherogenic effects. This protein has been shown to suppress the expression of class A scavenger receptors in macrophages, affect the nuclear factor (NF)-κB pathway and inhibit monocyte adhesion to aortic endothelial cells[6-8].

Address for correspondence: Yuko Katsuda, Molecular Genetics of Cardiovascular Disorders, Graduate School of Medical Science, Kanazawa University, 13-1 Takaramachi, Kanazawa 920-8640, Japan.
E-mail: y-katsuta@houju.or.jp
Received: May 23, 2006
Accepted for publication: October 14, 2006

Genetic variations in the human adiponectin gene, especially two single nucleotide polymorphisms (SNPs) (+45T>G and +276G>T), have been reported to be associated with obesity, insulin resistance[9], type 2 diabetes[10, 11], and coronary artery disease[12]. Hara *et al.* reported that these two SNPs were associated with insulin resistance, indicating the pathogenesis of type 2 diabetes[11]. The mechanism underlying insulin resistance in type 2 diabetes is not fully understood, but many studies in nondiabetic populations have addressed the importance of upper body fat distribution. However, the association between these SNPs and body fat distribution has not been investigated. Based on these previous findings, it has recently been reported that the G allele of SNP45 was associated with susceptibility to coronary artery disease independent of conventional risk factors[12]. Although, the mechanism is not clear, we hypothesized that SNP45 could modify body

fat distribution and lead to more accumulation of visceral adipose tissue, resulting in metabolic abnormalities and the development of atherosclerosis in the process of increasing adipose tissue. To determine the validity of this hypothesis, we investigated the association of SNP45 with (1) various clinical and metabolic parameters, (2) body fat distribution, and (3) the progression of atherosclerosis using the plaque score of the carotid artery and maximum IMT in a group of Japanese obese patients.

Material and Methods

Subjects

Sixty-four Japanese obese subjects (40 men and 24 women, aged 54.2 ± 16.6 years, BMI 30.3 ± 5.3 kg/m^2), receiving medical checkups in our institute from 2002 to 2004, were recruited for this study. These included 49 patients with type 2 diabetes, among whom 24 were treated with oral hypoglycemic agents, 13 with insulin, and 12 with diet alone. Subjects with other endocrine diseases or significant renal or hepatic disease were excluded.

Obesity was defined as a body mass index (BMI) ≧25 kg/m^2, based on the criteria of the Japan Society for the Study of Obesity[13]. Diabetes mellitus was diagnosed according to World Health Organization criteria[14] and/or receiving treatment for diabetes mellitus. Informed consent was obtained from all subjects. This study was approved by the Ethics Committee of Kanazawa University.

Screening of Mutations in the Adiponectin gene

Genomic DNA was extracted from peripheral blood leukocytes using the standard procedure. Genotypes were determined at position 45 relative to the translation start site (corresponding to GenBank AB012163S1, 2, 3) by PCR, followed by allele-specific hybridization.

DNA fragments containing SNP45 (372 bp) were amplified by PCR from genomic DNA using primers 5'-GCAGCTCCTAGAAGTAGACTCTGCTG-3' and 5'-GGAGGTCTGTGATGAAAGAGGCC-3'. PCR products were incubated at 25℃ for 2 hours using *SmaI* (New England BioLabs Inc. UK). Digested products were separated by size on 3% agarose gel with ethidium bromide staining. The DNA segment from the G/G homozygote of SNP45 was digested into 209 and 163 bp fragments.

Laboratory Measurements

BMI was calculated as weight (in kilograms) divided by height (in meters) squared. Waist circumference at the umbilical level was measured in the exhalation phase of respiration while standing.

Venous blood samples were obtained after a 12-hour overnight fast. Serum total cholesterol (TC) and triglyceride (TG) were determined by enzymatic methods, and high-density lipoprotein cholesterol (HDL-C) levels were measured by a polyanion-polymer/detergent method. Serum immunoreactive insulin (IRI) was measured by enzyme-linked immunosorbent assay, blood glucose with the glucose oxidase method, and HbA_{1c} by high-pressure liquid chromatography. The insulin resistance index was calculated based on homeostasis model assessment (HOMA) [fasting glucose (mmol/L) × fasting insulin (μU/mL)/22.5][15]. Plasma adiponectin levels were measured with an enzyme-linked immunosorbent assay kit (Otsuka Pharmaceutical Co., Tokushima, Japan), and leptin was measured by radioimmunoassay.

Body Fat Distribution

All subjects underwent computed tomography (CT) at the umbilical level to measure the cross-sectional abdominal subcutaneous fat area (SFA) and visceral fat area (VFA) using Fat Scan (N2 System Corp, Osaka, Japan)[16]. The VFA/SFA ratio was calculated as visceral fat area divided by subcutaneous fat area.

Determination of Plaque Score and Max IMT

A high resolution B-mode ultrasonography unit (SS-A 370A; Toshiba; Tokyo) with a 7.5 MHz transducer was used to determine the plaque score of the carotid artery[17]. Carotid Intima-Media Thickness (IMT) was measured at each common carotid, carotid bulb, and internal carotid artery.

The maximum IMT (Max-IMT) was defined as the highest IMT value at any location in the near and far walls of the carotid arteries, including atheromatous plaques on both sides. We defined a plaque, focal IMT thickening, as an area where IMT ≧ 1.1 mm, and calculated the plaque score by totaling the maximum thickness of all plaques on the near and far walls of vessels in the scanned area[17].

Statistical Analysis

All data are shown as the mean ± SD. A chi-square test was used to confirm that the genotype frequency was in Hardy-Weinberg equilibrium and to compare differences. Continuous variables were compared by ANOVA after being adjusted for age, BMI, and sex. Univariate and stepwise regression analyses were employed to examine the association between the plaque score and clinical parameters. All statistical analyses were conducted with StatView 5.0 for Macintosh

Table 1. Genotype distribution and allele frequencies for the adiponectin gene SNP45

	SNP45 genotypes			Allele frequencie	
	T/T	T/G	G/G	T	G
n (%)	34 (53.1)	25 (39.1)	5 (7.8)	0.72	0.28
male (n=40)	23 (57.5)	13 (32.5)	4 (10.0)	0.74	0.26
female (n=24)	11 (45.8)	12 (50.0)	1 (4.2)	0.71	0.29

Table 2. Clinical characteristics according to adiponectin genotypes at position 45

	T/T	T/G+G/G	P
n (%)	34 (53.1%)	30 (46.9%)	
M/F	23/11	17/13	0.36
Age (years)	53±15	56±18	0.39
Type 2 diabetes (%)	73.5	73.3	0.98
BMI (kg/m^2)	30.7±6.3	29.4±3.6	0.56
Waist (cm)	103.3±14.2	103.2±13.0	0.37
HOMA-R	3.6±2.3	3.3±1.9	0.80
HbA_{1c} (%)	7.1±1.9	6.7±1.6	0.32
Total cholesterol (mg/dL)	211±35	204±43	0.44
Triglycerides (mg/dL)	152±104	151±82	0.80
HDL cholesterol (mg/dL)	46±10	45±13	0.35
Adiponectin (μg/mL)	5.5±2.3	6.8±4.5	0.26
Leptin (ng/mL)	10.8±6.4	14.1±12.3	0.07
Systolic blood pressure (mmHg)	131±19	135±20	0.34
Diastolic blood pressure (mmHg)	79±11	79±14	0.65
Subcutaneous fat area (cm^2)	275.4±127.5	246.5±94.6	0.32
Visceral fat area (cm^2)	140.5±56.6	151.1±51.0	0.06
V/S ratio	0.56±0.24	0.76±0.45	0.009
Max IMT	1.89±0.81	2.21±0.91	0.27
Plaque score	6.1±4.1	9.7±3.9	<0.001

NOTE. Values are the means± SD. Heterozygotes and homozygotes for minor alleles were combined for presentation.
Abbreviations: BMI=body mass index, HOMA-R=homeostasis model assessment of insulin resistance
*P values adjusted for age, sex, and body mass index.

(Abacus Concepts, Berkeley, CA). A P value of less than 0.05 was considered statistically significant. In stepwise analysis, an F value greater than 4 was significant.

Results

Genotypes and Allele Distribution of SNP45 of the Adiponectin gene

The genotype and allele frequencies of study subjects are shown in **Table 1**. Genotype distributions were in Hardy-Weinberg equilibrium at both loci, with T being the major allele. The frequency of the T allele of SNP45 was 72%, and the frequencies of the T/T genotype, T/G genotype, and G/G genotype were 53.1%, 39.1%, and 7.8%, respectively.

Clinical and Metabolic Characteristics of this Study According to SNP45 of the Adiponectin gene

Table 2 shows a comparison of clinical characteristics and body composition according to adiponectin genotypes. Subjects were divided into 45T/T homozygote and those carrying the G allele (45T/G and 45G/G).

No differences in sex, age, or the proportion with diabetes were observed between any groups. Plasma leptin levels tended to be higher in carriers of the 45G allele (10.8±6.4 vs. 14.1±12.3, P=0.07). Other variables (HbA_{1c}, plasma lipid, and plasma adiponectin levels) did not differ between these genotypes.

Table 3. Clinical characteristics according to gender

	men	women	*P*
n	40	24	
Age (years)	51 ± 16	60 ± 14	0.02
BMI (kg/m^2)	30.7 ± 6.3	29.4 ± 3.6	0.56
Waist (cm)	102.7 ± 13.7	104.2 ± 13.5	0.03
HOMA-R	3.6 ± 2.4	3.1 ± 1.3	0.76
HbA_{1c} (%)	6.7 ± 1.9	7.4 ± 1.5	0.14
Total cholesterol (mg/dL)	204 ± 40	216 ± 36	0.15
Triglycerides (mg/dL)	166 ± 108	132 ± 59	0.37
HDL cholesterol (mg/dL)	42 ± 9	53 ± 12	0.02
Adiponectin (μg/mL)	5.2 ± 2.5	7.6 ± 4.4	0.03
Leptin (ng/mL)	9.6 ± 9.2	16.8 ± 9.2	0.03
Systolic blood pressure (mmHg)	132 ± 19	135 ± 19	0.27
Diastolic blood pressure (mmHg)	80 ± 13	77 ± 9	0.65
Subcutaneous fat area (cm^2)	246.4 ± 129.1	287.6 ± 76.3	<0.001
Visceral fat area (cm^2)	158.0 ± 56.3	124.5 ± 43.1	0.002
V/S ratio	0.77 ± 0.41	0.47 ± 0.17	<0.001
Max IMT	2.09 ± 1.00	1.96 ± 0.61	0.18
Plaque score	8.1 ± 4.1	7.9 ± 5.0	0.41

NOTE. Values are the means ± SD. Heterozygotes and homozygotes for minor alleles were combined for presentation.
Abbreviations: BMI=body mass index, HOMA-R=homeostasis model assessment of insulin resistance
*P values adjusted for age and body mass index.

Table 4. Body fat distribution and PS according to adiponectin genotypes at position 45 in men and women

	men			women		
	T/T	T/G + G/G	*P*	T/T	T/G + G/G	*P*
VFA	147.1 ± 58.7	172.8 ± 50.8	0.005	126.7 ± 52.0	122.7 ± 36.1	0.763
SFA	273.4 ± 142.2	209.9 ± 101.8	0.007	279.8 ± 95.6	294.3 ± 58.8	0.091
V/S ratio	0.60 ± 0.26	1.00 ± 0.46	<0.001	0.49 ± 0.18	0.44 ± 0.16	0.262
PS	6.8 ± 4.2	9.5 ± 3.7	0.012	4.4 ± 4.0	10.8 ± 3.8	0.135

NOTE. Values are the means ± SD. Heterozygotes and homozygotes for minor alleles were combined for presentation.
Abbreviations: VFA=visceral fat area, SFA=subcutaneous fat area

Relationship between Genotypes and Body Fat Distribution

When we considered the VFA/SFA ratio as a marker of body fat distribution, it was significantly higher in carriers of the 45G allele (0.76 ± 0.45 vs. 0.56 ± 0.24, P = 0.009), whereas there were no associations between SFA and SNP45. VFA tended to be higher in carriers of the 45G allele than TT homozygote (151.1 ± 51.0 vs. 140.5 ± 56.6 cm^2, P = 0.06). Neither BMI nor waist circumference significantly differed between the two groups. Since there were sex differences in body fat distribution in this study (**Table 3**: men vs. women; VFA: 158.0 ± 56.3 vs. 124.5 ± 43.1, P = 0.002; SFA: 246.4 ± 129.1 vs. 287.6 ± 76.3, P < 0.001; V/S ratio: 0.773 ± 0.410 vs. 0.470 ± 0.176, P < 0.001), we performed separate analyses of the association between SNP45 and body fat distribution by sex (**Table 4**, **Fig. 1**). In men, SNP45 was associated with the VFA, SFA, and V/S ratio, whereas in women SNP45 was not associated with body fat distribution.

Furthermore, to evaluate the contribution of SNP45 to the V/S ratio in men, stepwise regression analysis was used (**Table 5**). Selected variables were age, BMI, SNP45, and adiponectin. The data showed that age, SNP45, and plasma adiponectin levels were independent determinants of the V/S ratio in men (R^2 = 0.588, P < 0.0001).

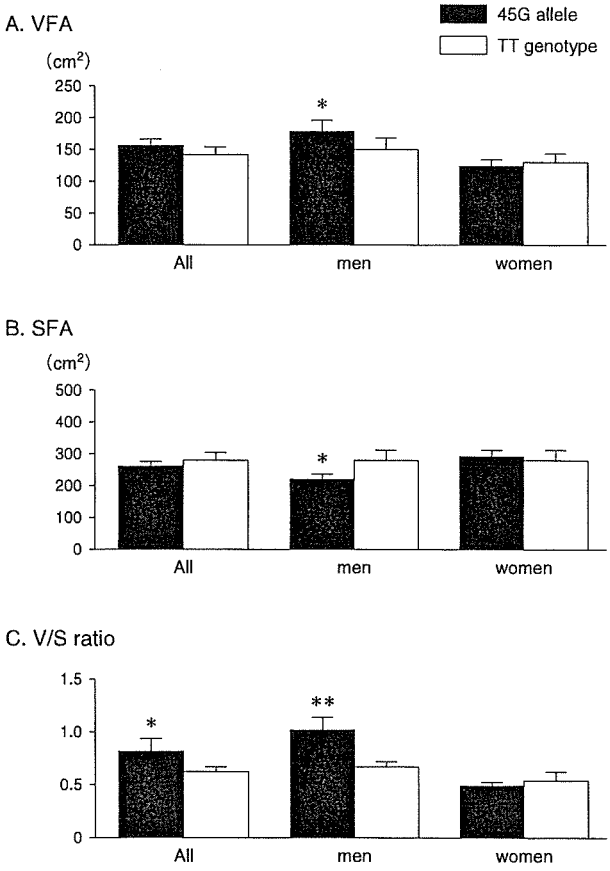

Fig. 1. Effect of SNP45 of the adiponectin gene on body fat distribution in all subjects, men and women

A. Effect of SNP45 on visceral fat area (VFA)
B. Effect of SNP45 on subcutaneous fat area (SFA)
C. Effect of SNP45 on VFA/SFA (V/F) ratio
Data are the means ± SE. $^{*}P<0.05$, $^{**}P<0.001$

Table 5. Stepwise regression analysis for determinant of V/S ratio in men

Factor	β	F-value
Age	0.017	35.763
SNP45*	0.340	24.945
Adiponectin	−0.073	13.688

$R^2=0.588$
*TT genotype=0, TG genotype=1, GG genotype=2

Table 6. Stepwise regression analysis for determinant of PS in men

Factor	β	F-value
Age	0.143	13.362
SNP45*	2.509	7.563

$R^2=0.372$
*TT genotype=0, TG genotype=1, GG genotype=2

Table 7. Correlation of PS to V/S ratio according to the genotype in men and women

	equation	r	p
men			
all	y=4.05x+4.71	0.39	0.02
G allele	y=3.22x+6.17	0.38	0.14
TT genotype	y=2.91x+4.93	0.17	0.49
women			
all	y=4.67x+5.85	0.17	0.47
G allele	y=12.00x+5.41	0.60	0.06
TT genotype	y=−2.57x+5.59	0.13	0.75

Relationship between Genotypes and Plaque Score of Carotid Artery

We investigated the effect of SNP45 on the plaque score and max IMT of carotid arteries. Carriers of the G allele had significantly greater PS than TT genotype after adjusting for age, sex, and BMI (10.0 ± 3.7 vs. 6.4 ± 4.2, $P<0.001$).

As shown in **Table 4**, SNP45 was associated with PS in men, and PS of the G allele tended to be higher than the TT genotype in women. To analyze the independent contribution of SNP45 to PS in men, stepwise regression analysis was applied (**Table 6**). Selected variables were age, BMI, V/S ratio, adiponectin, TC, HDL-C, systolic BP, and SNP45. The data showed that age and SNP45 were independent determinant of PS in men ($R^2=0.372$, $P=0.0007$).

Relationship between V/S Ratio and Plaque Score of Carotid Artery

To examine the effect of the V/S ratio on PS, we performed univariate analysis (**Table 7**).

There was a significant positive correlation between the V/S ratio and PS in men ($r=0.39$, $P=0.02$), whereas in women that correlation were not statistically significant ($r=0.17$, $P=0.47$).

Next, to investigate the impact of SNP45 on the association between the V/S ratio and PS, we subdivided into two groups according to the genotype of SNP45 in men and women. The V/S ratio tended to be associated with PS in the G allele in both men and women (men: $r=0.38$, $p=0.14$; women: $r=0.60$, $p=0.06$, respectively). In contrast, in subjects with the TT genotype, there was no relationship between the V/S ratio and PS.